Velocity Mapping Capabilities of Present and Future Altimeter Missions: The Role of High-Frequency Signals

P. Y. LE TRAON AND G. DIBARBOURE

CLS Space Oceanography Division, Ramonville Saint-Agne, France

(Manuscript received 18 September 2001, in final form 1 May 2002)

ABSTRACT

A detailed analysis of the velocity field mapping capabilities from existing and future multiple altimeter missions is carried out using the Los Alamos North Atlantic high-resolution model. The velocity mapping errors on the instantaneous fields and on 10-day averaged fields are systematically computed for all analyzed configurations. The T/P+ERS (Jason-1+ENVISAT) mapping error on the velocity remains acceptable (20%–30%) relative to the ocean signal. Mapping errors of 10-day averaged fields are twice as small, which shows that this configuration has a good potential for mapping lower frequencies of the velocity field. Compared to T/P+ERS, T/P+Jason-1 has a smaller error by about 20%–30% mainly because it is less sensitive to the aliasing of high-frequency signals. The mapping errors are twice as small with a three interleaved *Jason-1* configuration. One of the main findings of this study is the role of high-frequency signals that strongly limit the velocity mapping accuracy. The high-wavenumber high-frequency signals contribute to the total velocity variance by up to 20% in high eddy energy regions. This explains why the velocity mapping errors remain larger than about 15%–20% of the signal variance even for the four satellite configurations. This also explains why they do not decrease with the number of satellites as rapidly as expected. The aliasing of high-frequency signals is also a very serious issue. The high-frequency signals can induce large erroneous or inconsistent gradients between neighboring or crossing tracks. This strongly impacts the velocity estimation and explains why the meridional velocity mapping errors are larger than the zonal velocity mapping errors for the T/P+ERS configuration. However, it is shown that these aliasing problems can be partly reduced if they are properly taken into account in the mapping procedure.

1. Introduction

In a recent paper, Le Traon et al. (2001a, hereafter LDD01) analyzed the sea level mapping capabilities of multiple altimeters using the Los Alamos North Atlantic high-resolution model (Smith et al. 2000). The Los Alamos Model (LAM) represents the mesoscale variability quite well and offered a unique opportunity for assessing the mapping capability of multiple altimeter missions. This paper provides an extension of LDD01 work focusing on the velocity mapping capabilities. Most of the studies carried out so far on the altimetry sampling characteristics have been limited to the sea level. Quantifying the velocity mapping capabilities of present and future altimeter missions is, however, a very important issue. First, velocity contrary to sea level is a variable directly related to ocean dynamics. Second, knowledge of the velocity field is required for a wide range of operational applications of oceanography (e.g., Flemming 2001b; Le Traon et al. 2001b).

The velocity field is the derivative of the sea level field (in the geostrophic approximation) and its mapping demands a much better space and time sampling. Le Traon and Dibarboure (1999) (hereafter LD99) have analyzed, in particular, the sea level and velocity formal mapping errors of multiple altimeter missions. They found that the velocity field formal mapping error is thus typically 3 times larger (in percentage of signal variance) than the sea level mapping error. The velocity calculation is also more sensitive to measurement noise and small-scale ageostrophic ocean signals (e.g., Zlotnicki et al. 1993). As shown by Le Traon et al. (1998), the mapping of the velocity field also requires taking into account the along-track correlated errors (e.g., due to orbit error, inverse barometer and tidal errors) as the calculation of sea level gradients from neighboring or crossing tracks is affected by these errors. In particular, the effect can be large when several altimeters are combined as the tracks are closer together and the gradients steeper. Same holds for large-scale high-frequency barotropic signals (e.g., Tierney et al. 2000); these signals are sampled at different phases along the different tracks and if this is not properly taken into account in the mapping procedure, they will have the same effect as along-track correlated errors.

Corresponding author address: Dr. P. Y. Le Traon, Head Oceanography Department, CLS Space Oceanography Division, 8-10, rue Hermes Parc Technologique du Canal, 31526 Ramonville Saint-Agne, France.
E-mail: pierre-yves.letraon@cls.fr

The objective of our study is thus to quantify the velocity mapping capabilities of present and future altimeter missions but also to analyze the effect of unresolved high-frequency signals on the velocity mapping.

The paper is organized as follows. Methods are explained in section 2. Results are presented and discussed in section 3. The impact of a better statistical characterization of high-frequency signals is analyzed in section 4. Section 5 summarizes the main findings of the study.

2. Analyzed configurations and methods

a. Analyzed configurations

We chose to analyze the following multiple altimeter configurations:

- two altimeters: T/P+ERS, T/P+Jason-1 (interleaved),
- three altimeters: T/P+Jason-1+ENVISAT, three interleaved Jason-1, and
- four altimeters: four interleaved *Jason-1*.

The T/P+ERS (and later on Jason-1+ENVISAT) is the existing two-satellite configuration for which a long time series (more than 10 yr) is already available. The T/P+Jason-1+ENVISAT is a three-satellite configuration that is likely to occur but over a limited time period. The T/P+Jason-1 (track separation 1.4°, no time separation), the three interleaved *Jason-1* (track separation 0.9°, no time separation), and the four interleaved *Jason* (track separation 0.7°, no time separation) correspond respectively to ''optimized'' two-, three-, and four-satellite configurations. Sensitivity studies to the choice of the time separation were conducted for these optimized configurations, but the results do not significantly depend on this choice. This should not be too surprising as the choice of time separation does not modify the resolved spectral range for frequencies lower than the Nyquist frequency (here 20 days^{-1}) (Tai 1998). They do not induce, however, the same aliasing and have different resolution capabilities for high-frequency signals ($>$20 days^{-1}) (see discussion in sections 3 and 4).

b. Methods

The LAM sea level outputs were provided to us every 3 days on a 1/10° Mercator grid. They were first transformed into sea level anomaly data by removing a 3-yr mean (1993–95). For each of the analyzed configurations, the model sea level anomaly fields were then subsampled along T/P, ERS (or ENVISAT), and *Jason-1* tracks and a random noise of 2 cm rms was added to the simulated altimeter data. As in LD99 and LDD01, the simulations will not take into account long wavelength errors (e.g., orbital, tidal, or inverse barometer correction errors) as these errors could be partly reduced prior to or during the mapping procedure by using the more precise mission (T/P and later on *Jason-1*) as a reference (e.g., Le Traon and Ogor 1998; Le Traon et al. 1998). This is demonstrated in section 3d where a sensitivity study to orbit error is carried out for the TP+ERS configuration.

The simulated datasets are then used to reconstruct the sea level anomaly (SLA) gridded fields using the space–time suboptimal interpolation method described in LDD01 and in the appendix. The method uses variable space correlation scales (zero crossing of correlation function) (ZC) and time correlation (*e*-folding time) (ET), which are intended to represent typical space and timescales of SLA as they can be observed from altimetry. The signal mapping (contrary to the formal error estimation) is not very sensitive, in any case, to these a priori choices when the constraint from the data is strong. This was quantified by LDD01 who showed that in the Gulf Stream area the variance of the sea level mapping error for the T/P+Jason-1 configuration varies by only ±10% for different choices of space and timescales ranging from 100 to 200 km and 10 to 20 days, respectively. Note that our ZC and ET choice at this latitude provides one of the smallest mapping errors. A similar result is found here for the velocity mapping error. Tests were also performed with a covariance model taking into account a propagation velocity (e.g., Kurugano and Kamachi 2000), and results were not significantly different than the ones derived from our nominal simulation.

The sea level and velocity mapping errors are defined here as the differences between the input LAM fields and the output fields reconstructed by the mapping technique described above from the model sampled as the satellites would. Both reconstructed and input fields were resampled to regular 1/10° by 1/10° grids for differencing. The velocity calculations for both input and reconstructed fields are only the geostrophic components, computed from sea level gradients (numerically from finite centered differences). In practice, the comparison was made over a 6-month period (1993) with maps calculated every 9 days; that is, we compared a total of 20 maps. The calculations were done on a large area from 20° to 60°N and 75° to 10°W, that is, covering the full North Atlantic.

c. Role of high-frequency signals and mapping of 10-day averaged fields

LDD01 have shown that sea level mapping errors derived from the simulation using the LAM fields were larger than the ones derived from LD99 formal error analysis (by a factor of 1.5 to 2). This was mainly due to high-frequency signals. These signals were derived here from the differences between the LAM instantaneous and 10-day averaged fields. The LAM 10-day averaged fields were obtained with a Loess filter with a cutoff frequency of 16 days^{-1} (which chiefly corresponds to 10-day averages) (see Schlax and Chelton 1992).

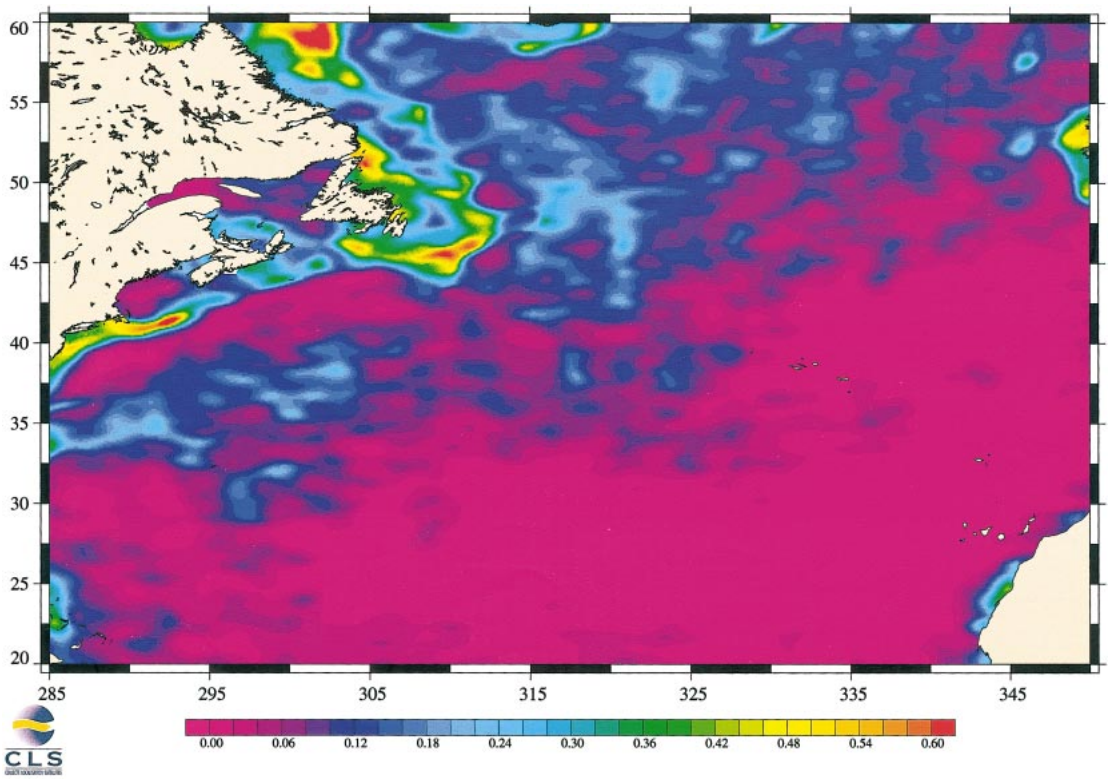

FIG. 1. Relative energy (expressed in percentage of total variance) of high-frequency signals for the LAM zonal velocity. The high-frequency signals were derived from the differences between the LAM instantaneous and 10-day averaged fields.

In areas with large mesoscale variability, they represent 5%–10% of the total sea level variance (see also Minster and Gennero 1995) and are associated with high wavenumbers. They account for 15%–20% of the total velocity variance (Fig. 1). In shallow and high-latitude regions, these high-frequency signals account for up to 30%–40% of the total sea level and velocity variance; there, part of these signals correspond to large-scale barotropic motions.

To better analyze the impact of high-frequency signals on the sea level and velocity mapping, we systematically computed for all analyzed configurations the mapping errors on the instantaneous fields (as in LDD01) and on 10-day averaged fields. To map 10-day averaged fields, the a priori measurement noise was increased by 10% (which is a rough estimate of the contribution of high-frequency signals, see, e.g., LDD01) (the impact of a better statistical characterization of high-frequency signals will be presented in section 4). The estimated fields were then compared to the model 10-day averaged fields.

Note that the objective analysis technique could have been modified to directly estimate 10-day averaged fields [see Bretherton et al. (1976) and an application to coastal zone color scanner (CZCS) observations by Chelton and Schlax (1991)]. It is easy to show, however, that our implementation is exactly equivalent to this theoretical approach if we assume that our initial covariance model does not include the contribution of high-frequency signals.

d. Illustration of the methodology

To illustrate the methodology, we show in Fig. 2a the LAM zonal velocity anomaly for a given day. Figure 2b shows the corresponding mapping error for the ERS configuration. The mapping error of the 10-day averaged field is shown in Fig. 2c. One can note that while the T/P+ERS configuration captures the main large spatial scale velocity signals, it misses the smaller scales (wavelengths below 200 km). These signals are mainly associated with small timescales and as a result the mapping error of the 10-day averaged fields is much smaller.

3. Results and discussion

In this section, the main statistical results are first presented. A general description and interpretation of mapping errors is then given. We then detail the results specific to each of the different analyzed configurations.

a. Statistical results

The rms of the zonal and meridional velocity mapping errors over the 6-month period both for the in-

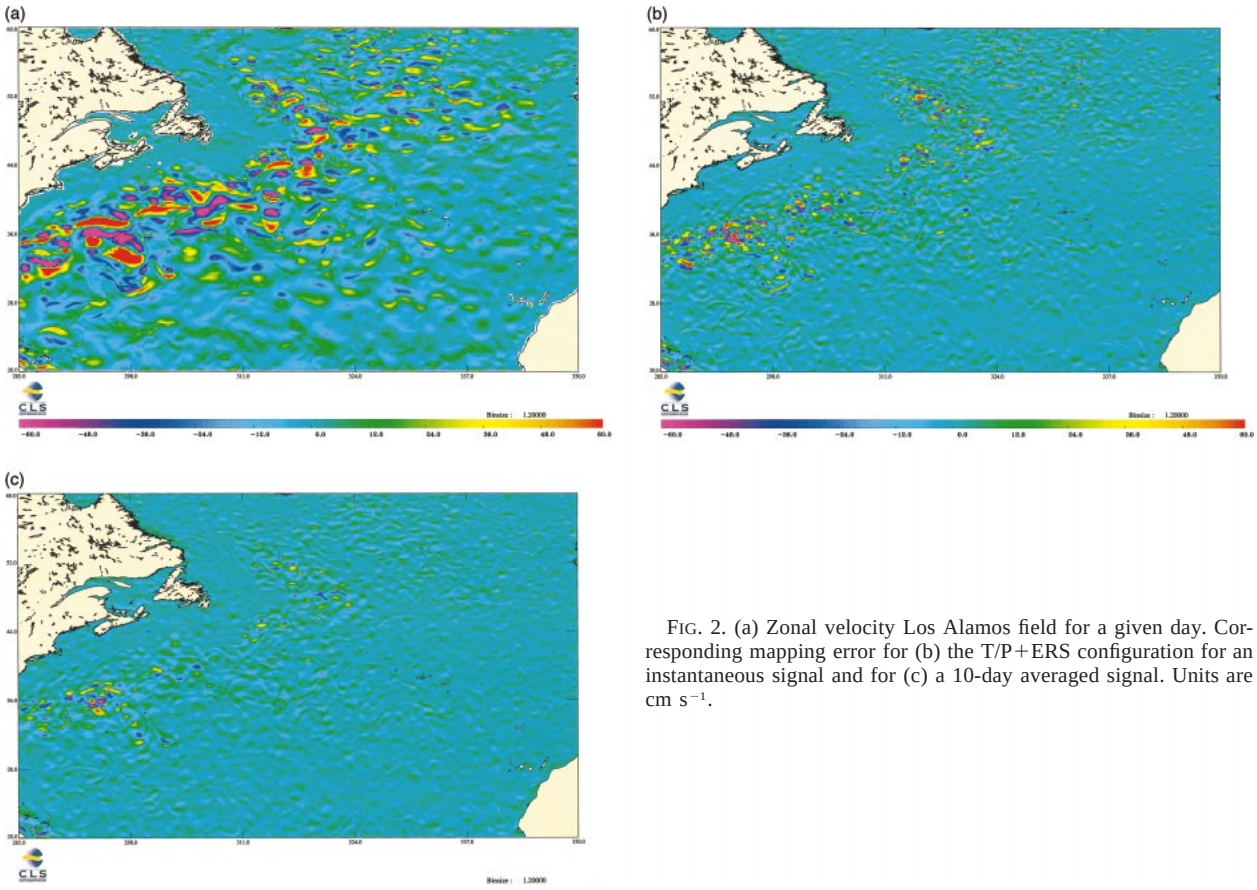

FIG. 2. (a) Zonal velocity Los Alamos field for a given day. Corresponding mapping error for (b) the T/P+ERS configuration for an instantaneous signal and for (c) a 10-day averaged signal. Units are cm s^{-1}.

stantaneous and 10-day averaged signals were computed for all the configurations listed in section 2. The rms of the zonal velocity mapping errors for T/P+ERS, Jason-1+ENVISAT, three interleaved Jason-1, and four interleaved Jason-1 are shown in Fig. 3 respectively. Mapping errors for 10-day averaged signals are shown in Fig. 4. They can be compared to the rms LAM zonal velocity over the same 6-month period (Fig. 5).

Mapping errors depend on many factors: sampling characteristics, amplitude, space and timescales of mesoscale ocean signals, relative energy of high-frequency signals and measurement noise (only for low variability regions). Except for noise, all these characteristics vary geographically. As a result, the mapping errors show large and complex geographical variations. The main effect is, of course, related to the variations in eddy energy. To partly remove this effect, the quadratic relative sea level, zonal and meridional velocity mapping errors (i.e., the ratio of the mapping error variance over the ocean signal variance) were also calculated. Table 1 summarizes the results obtained for regions where the rms sea level variability is larger than 15 cm rms. This allows us to analyze the mapping capabilities for regions whose dynamics are dominated by mesoscale variability. Mean relative mapping errors are given both for ''instantaneous'' and 10-day averaged signal mapping.

b. *General description of mapping errors—The role of high-frequency signals*

The velocity mapping errors remain larger than about 15%–20% of the signal variance even for the four-satellite configuration. They also do not decrease with the number of satellites as rapidly as expected (e.g., from a formal error analysis as performed by LD99). As shown by LDD01 for sea level, the effect is mainly related to high-frequency signals. In regions dominated by mesoscale variability, the high-frequency velocity signals have a variance of about 15%–20% of the total velocity variance (Fig. 1); they are mainly associated with high-wavenumber signals. Such signals cannot be resolved with any of the analyzed multiple altimeter configurations. To illustrate the contribution of high-frequency signals to the mapping error, the variations of the relative mapping errors according to the relative energy of high-frequency signals are shown in Fig. 6 for sea level, zonal velocity, and meridional velocity. Figure 6 shows that the relative mapping errors for all

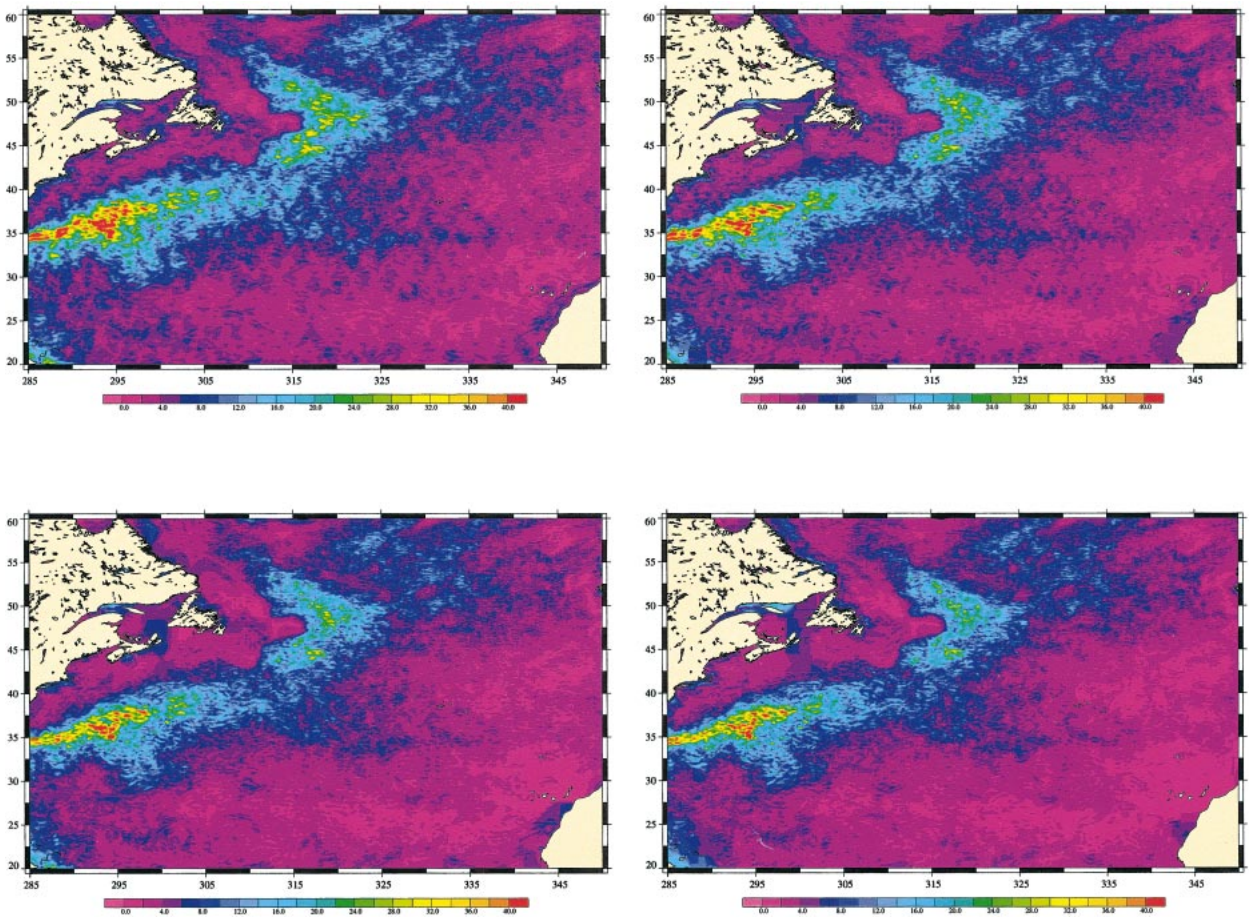

FIG. 3. Rms zonal velocity mapping error for (top left) T/P+ERS, (top right) T/P+Jason-1+ENVISAT, (bottom left) three interleaved *Jason-1*, (bottom right) and four interleaved *Jason-1*. Units are cm s^{-1}.

configurations are almost linearly related to the relative energy of high-frequency signals both for sea level and velocity. Note that the velocity mapping errors are about twice as large as the relative energy of high-frequency signals while the ratio is about one for sea level. This probably means that lower frequencies of the velocity field are also poorly resolved by the different configurations and/or that aliasing problems accentuate the effect of high-frequency signals (see discussion below).

Sea level and velocity relative mapping errors also generally increase with latitude by a factor of 2 to 3 (not shown). These variations are mainly due to an increase of the relative energy of high-frequency signals with latitude (see Fig. 1). The eddy spatial scales also decrease with latitude, but as the distance between the satellite tracks also decreases, this effect is less important. Variations of the track inclination also impact the zonal and velocity mapping errors, but the effect should be of the order of 10% (see LD99). Note that, for a given sea level variance, the variation of the Coriolis parameter with latitude does not impact the relative velocity mapping errors (see LD99).

The mapping errors on 10-day averaged fields are smaller than the mapping errors on the instantaneous fields by a factor of 2 to 4. Multiple altimeter configurations thus allow a very good mapping of 10-day averaged velocity fields. This also shows again that a large fraction of the error on instantaneous velocity fields is due to high-frequency signals. The fraction is larger when more satellites are used.

The high-frequency signals do not impact the sea level and velocity in the same way. In high eddy energy regions, the high-frequency signals are associated with high wavenumbers (see LDD01); they induce more error on the velocity field as they contribute much more (by a factor of 4) to the total variance. For example, the contribution of high-frequency signals to the total signal variance in the Gulf Stream area is between 5% and 10% for sea level but is about 20% for velocity. At high latitudes, the large-scale barotropic motions have a large impact on the sea level mapping error as they contribute by up to 50% to the total sea level variance (see LDD01). They contribute much less to the velocity field variance (as they are of large scales) and one may thus

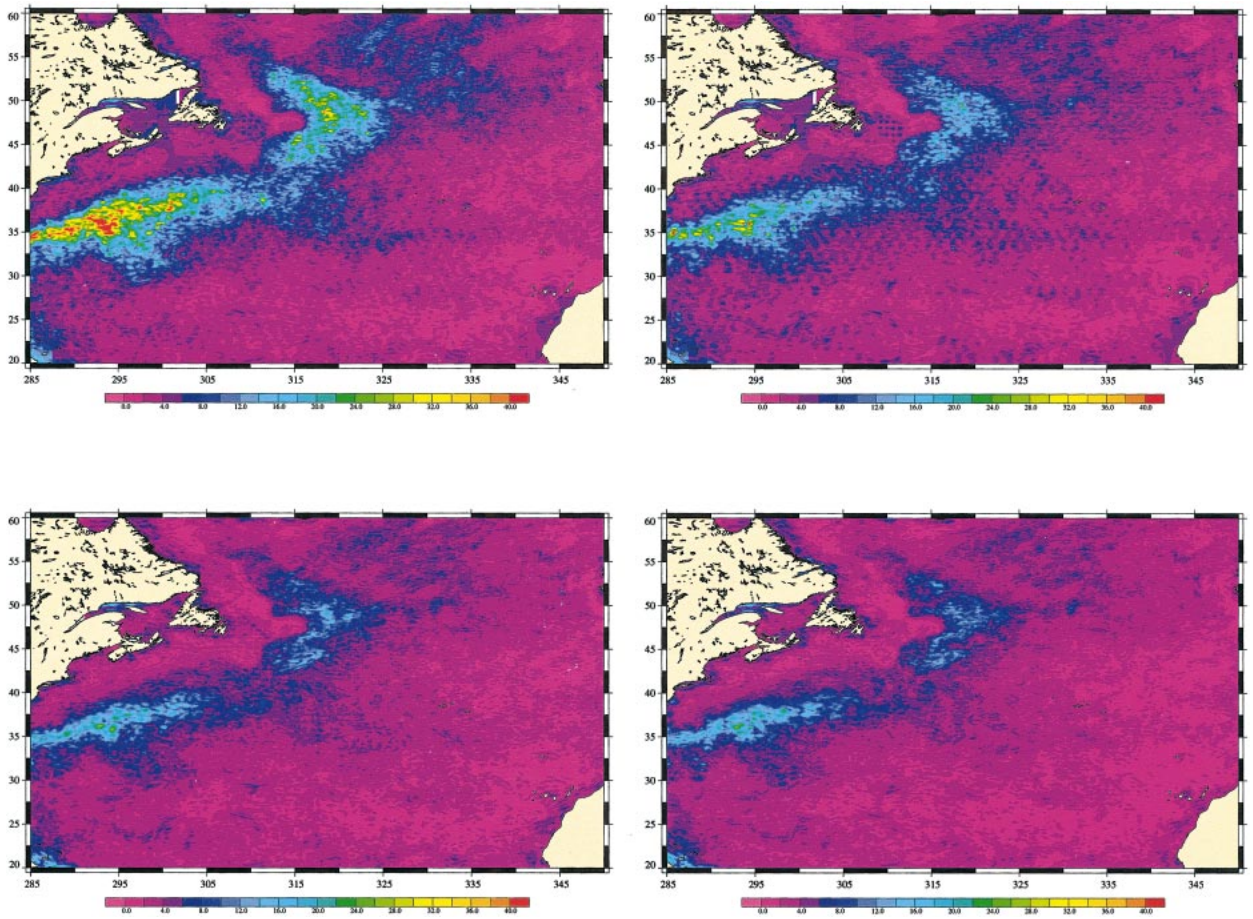

FIG. 4. Same as Fig. 3 but for a 10-day average signal mapping error.

have expected a much smaller impact on the velocity mapping error. They induce, however, serious aliasing problems because they sample the neighboring and crossing tracks at different times and thus create artificial sea level gradients (see Le Traon et al. 1998). Thus both large-scale and high-wavenumber high-frequency signals strongly impact the velocity field mapping.

The high-frequency signals explain why the meridional velocity mapping errors (instantaneous and 10-day averaged) are larger than the zonal velocity mapping errors for the T/P+ERS and to a less extent for the Jason-1+ENVISAT configurations. The ERS/ENVISAT track inclination favors a better estimation of the zonal velocity, but the meridional velocity mapping error should be only 10%–20% larger than the zonal ve-

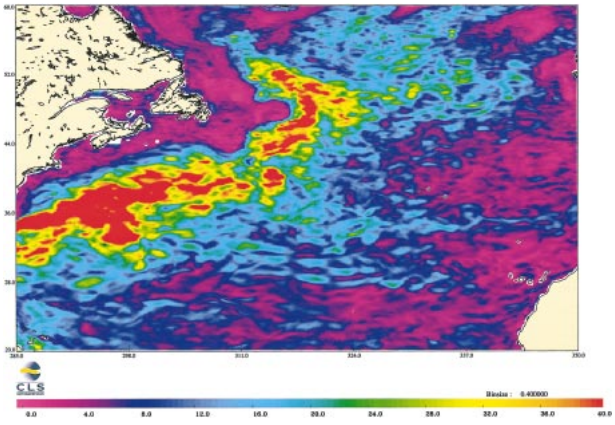

FIG. 5. Rms of the LAM zonal velocity. Units are cm s^{-1}.

TABLE 1. Sea level (H), zonal (U), and meridional (V) velocity mean mapping errors for regions with rms sea level variability larger than 15 cm. Errors expressed as percentage of the mean sea level and velocity variance. They are given both for instantaneous and 10-day averaged signal mapping.

	H	U	V
ERS+T/P	7.2 / 3.2	26.3 / 9.9	35.0 / 13.5
Jason-1+T/P	5.0 / 2.0	21.6 / 7.4	24.2 / 8.9
T/P+Jason-1+ENVISAT	4.2 / 1.8	19.6 / 6.9	22.3 / 8.3
Three interleaved Jason-1	3.7 / 1.5	17.9 / 5.3	20.6 / 6.3
Four interleaved Jason-1	3.4 / 1.0	16.9 / 3.9	20.1 / 4.5

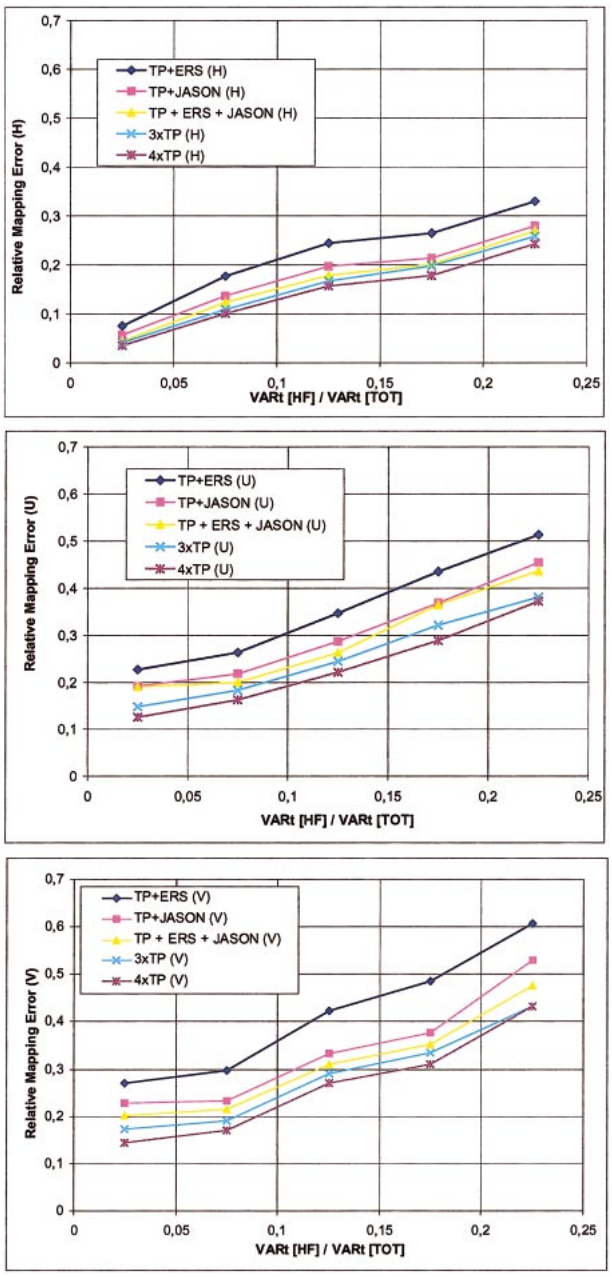

FIG. 6. Relative mapping error for sea level and zonal and meridional velocities according to the relative energy of sea level and velocity high-frequency signals.

locity mapping error (see LD99). The effect observed here is larger than 30%. The aliased high-frequency signals (both large-scale and high wavenumbers) induce large erroneous gradients between neighboring ERS/ENVISAT tracks because the tracks are close apart and sampled at very different times (subcycles of 16 and 19 days). This strongly impacts the meridional velocity estimation. The aliased high-wavenumber and high-frequency signals also induce inconsistent sea level gradients along ascending and descending tracks at crossover points. Given the ERS/ENVISAT track inclination, these inconsistencies will also impact mainly the meridional velocity estimation.

c. *Results from the two-satellite configurations*

The T/P+ERS configuration deserves particular attention as this is the existing and future (Jason-1 and ENVISAT) two-satellite configuration. The mapping error on the velocity remains acceptable (20%–30%) relative to the ocean signal. Mapping errors of 10-day averaged fields are twice as small, which shows that the T/P+ERS configuration has a good potential for mapping the lower frequencies of the velocity field. Mapping errors also depend on latitude (not shown) and generally vary from 20% at 20°N to up to 50% at 60°N. This is consistent with the result found by Ducet et al. (2000). From the comparison of the eddy kinetic energy (EKE) derived from drifter trajectories and combined ERS maps, they found that T/P+ERS maps had an EKE underestimated by more than 30% at high latitudes. As explained above, the meridional velocity mapping errors are larger than the zonal velocity variance by up to 30% due to the aliasing of high-frequency signals. This may explain why Ducet et al. (2000) found a slight overestimation of T/P+ERS meridional velocity variance in the Gulf Stream area compared to drifter data.

Compared to T/P+ERS mapping error, T/P+Jason error is smaller by about 20%–30% for the instantaneous signal. This is larger than the results found by LD99. The T/P+Jason-1 configuration with its 10-day repeat period almost provides a synoptic sampling of the ocean. It is thus less sensitive to the aliasing of high-frequency signals. This also explains why there is a better performance of this configuration for mapping 10-day averaged fields.

d. *Results from the three- and four-satellite configurations*

The mapping errors are much smaller than the signal over most of the areas. The configurations with more than two satellites have very small mapping errors on 10-day averaged fields, which means that the mapping errors on instantaneous fields are dominated by high-frequency signals. The optimized three satellite configuration (three Jason-1) performs significantly better than the nonoptimized configuration (T/P+Jason-1+ENVISAT). The improvement is not as large, however, as the one observed for the two-satellite configurations. Compared to T/P+ERS, a three interleaved Jason allows thus a reduction of the sea level and velocity mapping error by a factor of about 2. As noted in section 3b, even the four-satellite configuration cannot resolve the high-frequency velocity signals. This is the reason why

there is a limited reduction of velocity mapping error with the four-satellite configuration.

e. Impact of orbit errors

For the above simulations, only instrumental noise was considered. We assumed that long wavelength errors and, in particular, orbit errors should not significantly impact our results if they are properly taken into account in the mapping procedure. This is demonstrated here for T/P+ERS configuration. An orbit error of 3 cms rms for ERS and 1 cm rms for T/P was simulated. The orbit error was assumed to be at one cycle per revolution with a random amplitude and phase for the different tracks and cycles. The impact on the sea level and velocity mapping errors is first quantified when the orbit error is not taken into account in the mapping procedure. The orbit error is then explicitly taken into account in the mapping procedure following the method proposed by Le Traon et al. (1998) (see also the appendix). Mean relative sea level and velocity mapping errors according to rms sea level variability are shown in Fig. 7. When orbit error is not taken into account in the mapping procedure, the impact can be very large, in particular, in low eddy energy regions. As expected (see discussion in section 3c), the effect is much larger on the meridional velocity. When the orbit errors are taken into account in the mapping, they do not significantly impact our results. We actually get slightly better results for high-eddy energy regions because when we take into account along-track biases, we also partly reduce high-frequency aliasing problems (see section 4).

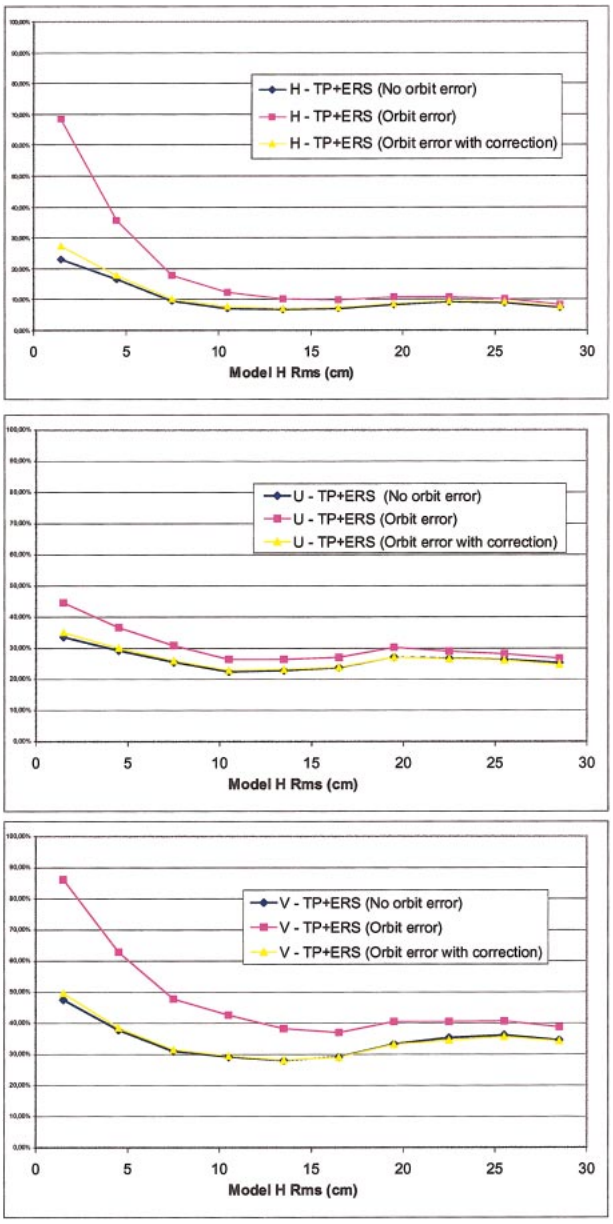

FIG. 7. Impact of orbit error on sea level, zonal, and meridional velocity mapping errors for the TP+ERS configuration. Mean relative mapping errors are given according to rms sea level variability for the reference simulation (no orbit error), the simulation with orbit error and the simulation when orbit error is taken into account in the mapping procedure.

4. Impact of a better statistical characterization of high-frequency signals

One of the main findings of these simulations is the importance of high-frequency signals in the mapping errors. They limit our ability to map the velocity field with an accuracy better than 20% of the signal variance. They also impact the mapping of the lower-frequency velocity signals because of aliasing problems. We used a crude parametrization of the high-frequency signals in the 10-day averaged field mapping procedure (uncorrelated noise of 10%). We analyze here the impact of a better statistical characterization of these signals for the T/P+ERS configuration. The objective is to better filter out the high-frequency signals and thus reduce the aliasing problems for the estimation of 10-day averaged fields. As will be seen below, this also reduces the mapping errors on instantaneous signals.

To better take into account the high-frequency signals, we introduce in the mapping procedure both a small-scale and large-scale correlated noise. The small-scale (respectively, large-scale) noise is supposed to correspond to the variance of high-wavenumber (respectively, large-scale) high-frequency signals. The small-scale noise was assumed to be correlated over a distance of 50 km (it should correspond to small eddies and meanders) and uncorrelated between the tracks and cycles. The large-scale noise was assumed to be an along-track bias uncorrelated between the other tracks and cycles (see Le Traon et al. 1998; see also the appendix). These two spatially variable noise variances were determined

TABLE 2. Impact of the two paramatrization of the high-frequency signals on sea level (H), zonal (U), and meridional (V) velocity mean mapping errors. Errors expressed as percentage of the mean sea level and velocity variance are given both for instantaneous and 10-day averaged signal mapping.

	H	U	V
Refference simulation	7.2 / 4.5	26.3 / 13.9	35.0 / 21.1
H.F. = crude parameterization	6.8 / 3.2	25.0 / 9.9	29.6 / 13.5
H.F. = improved parameterization	6.8 / 3.1	24.6 / 9.6	28.5 / 12.4

from an analysis of the LAM high-frequency signals as follows.

- The differences between the LAM instantaneous and 10-day averaged (obtained with a Loess filter as explained in section 2d) fields were calculated to generate a time series of maps of high-frequency sea level signals.
- A 2D spatial Loess filter was then applied to retain only wavelengths larger than 1000 km. These signals were considered as the high-frequency large-scale (barotropic) motions.
- The remaining signals were considered as the high-wavenumber high-frequency signals.

Table 2 gives the sea level and velocity mean mapping errors for our reference simulation (no additional noise due high-frequency signals), the crude parameterization simulation (10% noise due to high-frequency signals) and the improved parameterization simulation (small-scale and large-scale noise due to high-frequency signals). As in section 3, only regions where the rms sea level variability is larger than 15 cm rms are considered. Errors are given both for instantaneous and 10-day averaged signal mapping.

Taking into account the ''noise'' due to high-frequency signals very significantly improves the mapping of 10-day averaged fields (see Table 2). The improvement is particularly large for the meridional velocity mapping (almost a factor 2) because it strongly reduces the aliasing problem. Compared to the crude parameterization, the improved parameterization allows a better mapping. It reduces again the difference between zonal and meridional velocity variance. The gain is not very large, however, which means that the crude parameterization is already very effective.

More surprisingly, adding a noise due to high-frequency signals also significantly improves the mapping of instantaneous fields (see Table 2). This mainly holds for the meridional velocity mapping, which is very sensitive to aliasing problems. As the high-frequency signals cannot be mapped, it is thus preferable (at least for the T/P+ERS configuration) to filter them out even to estimate the best instantaneous velocity signals. Larger errors are introduced because of aliasing problems.

5. Conclusions

A detailed analysis of the velocity field mapping capabilities from existing and future altimeter missions has been carried out using the Los Alamos North Atlantic high-resolution model. Existing multiple altimeter configurations (T/P+ERS or Jason-1+ENVISAT) as well as constellations of three or four satellites were analyzed.

The T/P+ERS (Jason-1+ENVISAT) mapping error on the velocity remains acceptable relative to the ocean signal (20%–30%). Mapping errors of 10-day averaged fields are twice as small, which shows that this configuration has a good potential for mapping the lower frequencies of the velocity field. Compared to T/P+ERS mapping error, T/P+Jason-1 error is smaller error by about 20% to 30% for the instantaneous signal. The Jason-1 configuration almost provides a synoptic sampling of the ocean and is thus less sensitive to the aliasing of high-frequency signals. The configurations with more than two satellites have very small mapping errors on 10-day averaged fields, which means that the mapping errors on instantaneous fields are dominated by high-frequency signals. Compared to T/P+ERS, a three interleaved Jason thus allows a reduction of the sea level and velocity mapping error by a factor of about 2.

The main finding of this study is the role of high-frequency signals. The high-wavenumber high-frequency signals contribute to the total velocity variance by up to 20% in high eddy energy regions. Since these signals cannot be resolved with any of the analyzed configurations, they strongly limit the mapping accuracy. This explains why the velocity mapping errors remain larger than about 15%–20% of the signal variance even for the four satellite configurations. The aliasing of high-frequency signals is also a very serious issue. The high-frequency signals can induce large erroneous gradients between neighboring tracks and inconsistent sea level gradients along ascending and descending tracks at crossover points. This also strongly impacts the velocity mapping error and explains why the meridional velocity mapping errors are larger than the zonal velocity mapping errors for the T/P+ERS configuration. Both large-scale and high-wavenumber signals contribute to the aliasing problems. Thus even if the large-scale high-frequency signals (e.g., barotropic signals) do not contribute much to the total velocity variance, they can strongly impact the velocity mapping in particular in low eddy energy regions [note that the large-scale signals could be partly corrected for using barotropic models (e.g., Tierney et al. 2000; Hirose et

al. 2001)]. These aliasing problems can be partly reduced, however, if they are properly taken into account in the mapping procedure. We showed that a better statistical characterization of high-frequency signals allows a better mapping of sea level and velocity from T/P and ERS data both for instantaneous and 10-day averaged fields. These results have a direct implication for improving the processing and interpretation of the entire T/P+ERS and later on Jason-1+ENVISAT time series.

Acknowledgments. We thank R. Smith for providing us with the Los Alamos model outputs. The study was funded by CNES under Contract CNES/CLS No. 731/CNES/00/8435/00.

APPENDIX

Details on the Objective Analysis Method

The problem is to determine the value of a field θ [θ is here the Sea Level Anomaly (SLA)] at a point $\times$ in time and space, given measurements of θ unevenly spread over time and space $\Phi_{\text{obs}i}$, $i = 1, \ldots, n$. The best least squares linear estimator $\theta_{\text{est}}(x)$ is given by (see Bretherton et al. 1976)

$$\theta_{\text{est}}(x) = \sum_{i=1}^{n} \sum_{j=1}^{n} A_{ij}^{-1} C_{xj} \Phi_{\text{obs}}^{i},$$

with $\Phi_{\text{obs}^i} = \Phi_i + \varepsilon_i$, where Φ_i is the true value and ε_i the measurement error. Here A is the covariance matrix for the observations, and C the covariance vector for the observations and the field to be estimated: $A_{ij} = \langle \Phi_{\text{obs}^i} \Phi_{\text{obs}^j} \rangle = \langle \Phi_i \Phi_j \rangle + \langle \varepsilon_i \varepsilon_j \rangle$ $C_{xi} = \langle \theta(x) \Phi_{\text{obs}^i} \rangle = \langle \theta(x) \Phi_i \rangle$.

The measurement error is assumed to be uncorrelated with the signal. The SLA variance VAR_x is derived from the Los Alamos model fields. The following space–time correlation function $C(r, t)/\text{VAR}_x$ of the SLA field is used:

$$C(r, t) = [1 + ar + 1/6(ar)^2 - 1/6(ar)^3] \times \exp(-ar) \exp(-t^2/T^2),$$

where r is distance, t time, $\text{ZC} = 3.34/a$ is the space correlation radius (first zero crossing of C), and T the e-folding timescale. Here ZC and T are set as follows:

$$\text{ZC} = 50 + 250\left(\frac{900}{\text{Lat}^2 + 900}\right) \text{km},$$

where ''Lat'' stands for latitude (in deg),

$$\text{ET} = 15 \text{ days}.$$

These scales are intended to represent typical space and timescales of the SLA and, in particular, the reduction in space scale of mesoscale eddies with latitude.

Given the high number of altimeter measurements, the method is suboptimal: only useful data, that is, values close to the point to be estimated, are used. In practice, this comes down to selecting data in a space–time subdomain. For this application, only data within an ellipsoid of influence with a radius of ZC and T are used.

The reference simulations used a white measurement noise. To take into account orbit errors or high-frequency large-scale signals, a correlated noise is introduced by modifying the error covariance, $\langle \varepsilon_i \varepsilon_j \rangle$ as follows (see Le Traon et al. 1998):

$$\langle \varepsilon_i \varepsilon_j \rangle = \begin{cases} \delta_{i,j} b^2 & \text{for points i, j not on the same track or in the same cycle} \\ \delta_{i,j} b^2 + E_{\text{LW}} & \text{for points i, j on the same track and in the same cycle,} \end{cases}$$

where b^2 is the variance of the white measurement noise and E_{LW} is the variance of the long wavelength error.

The long wavelength error is therefore assumed constant along the tracks over the ellipsoid of influence. To allow a better separation of signal and large-scale errors, the sphere of influence is extended to 3 ZC in latitude and longitude when an along-track correlated noise is introduced. We thus assume that over such distances (of the order of 1000 km), orbit errors or high-frequency signals can be modeled as a bias.

REFERENCES

Bretherton, F., R. Davis, and C. Fandry, 1976: A technique for objective analysis and design of oceanographic experiments applied to MODE-73. *Deep-Sea Res.,* **23,** 559–582.

Chelton, D. B., and M. G. Schlax, 1991: Estimation of time averages from irregularly spaced observations: With application to coastal zone color scanner estimates of chlorophyll concentration. *J. Geophys. Res.,* **96,** 14 669–14 692.

Ducet, N., P. Y. Le Traon, and G. Reverdin, 2000: Global high resolution mapping of ocean circulation from the combination of TOPEX/Poseidon and *ERS-1/2. J. Geophys. Res.,* **105,** 19 477–19 498.

Flemming, N. C., 2001: Dividends from investing in ocean observations: A European perspective. *Observing the Oceans in the 21st Century*, C. J. Koblinsky and N. R. Smith, Eds., GODAE Project Office and Bureau of Meteorology, Melbourne, Australia, 66–84.

Hirose, N., I. Fukumori, V. Zlotnicki, and R. M. Ponte, 2001: Modeling the high-frequency barotropic response of the ocean to atmospheric disturbances: Sensitivity to forcing, topography, and friction. *J. Geophys. Res.,* **106,** 30 987–30 996.

Kuragano, T., and M. Kamachi, 2000: Global statistical space–time scales of oceanic variability estimated from the TOPEX/Poseidon altimeter data. *J. Geophys. Res.,* **105,** 955–974.

Le Traon, P. Y., and F. Ogor, 1998: *ERS-1/2* orbit improvement using TOPEX/Poseidon: The 2 cm challenge. *J. Geophys. Res.,* **103,** 8045–8057.

——, and G. Dibarboure, 1999: Mesoscale mapping capabilities from multiple altimeter missions. *J. Atmos. Oceanic Technol.,* **16,** 1208–1223.

——, F. Nadal, and N. Ducet, 1998: An improved mapping method of multisatellite altimeter data. *J. Atmos. Oceanic Technol.,* **15,** 522–534.

——, G. Dibarboure, and N. Ducet, 2001a: Use of a high-resolution model to analyze the mapping capabilities of multiple-altimeter missions. *J. Atmos. Oceanic Technol.,* **18,** 1277–1288.

——, M. Rienecker, N. Smith, P. Bahurel, M. Bell, H. Hurlburt, and P. Dandin, 2001b: Operational oceanography and prediction—A GODAE perspective. *Observing the Oceans in the 21st Century*, C. J. Koblinsky and N. R. Smith, Eds., GODAE Project Office and Bureau of Meteorology, Melbourne, Australia, 529–545.

Minster, J. F., and M. C. Gennero, 1995: High-frequency variability of western boundary currents using *ERS-1* three-day repeat altimeter data. *J. Geophys. Res.*, **100,** 22 603–22 612.

Schlax, M. G., and D. B. Chelton, 1992: Frequency domain diagnostics for linear smoothers. *J. Amer. Statist. Assoc.*, **87,** 1070–1081.

Smith, R. D., M. E. Maltrud, F. O. Bryan, and M. W. Hecht, 2000: Numerical simulation of the North Atlantic ocean at 1/10°. *J. Phys. Oceanogr.*, **30,** 1532–1561.

Tai, C. K., 1998: On the spectral ranges that are resolved by a single satellite in exact repeat sampling mode. *J. Atmos. Oceanic Technol.*, **15,** 1459–1470.

Tierney, C., J. Wahr, F. Bryan, and V. Zlotnicki, 2000: Short-period oceanic circulation: Implications for satellite altimetry. *Geophys. Res. Lett.*, **27,** 1255–1258.

Zlotnicki, V., G. Siedler, and B. Klein, 1993: Can the weak surface currents of the Cape Verde frontal zone be measured with altimetry. *J. Geophys. Res.*, **98,** 2485–2493.